

Fallback accretion on to a newborn magnetar: long GRBs with giant X-ray flares

S. L. Gibson,^{1★} G. A. Wynn,^{1★} B. P. Gompertz^{2,3★} and P. T. O’Brien¹

¹*Department of Physics and Astronomy, University of Leicester, University Road, Leicester LE1 7RH, UK*

²*Space Telescope Science Institute, 3700 San Martin Drive, Baltimore, MD 21218, USA*

³*Department of Physics, University of Warwick, Coventry CV4 7AL, UK*

Accepted 2018 May 22. Received 2018 May 21; in original form 2018 February 8

ABSTRACT

Flares in the X-ray afterglow of gamma-ray bursts (GRBs) share more characteristics with the prompt emission than the afterglow, such as pulse profile and contained fluence. As a result, they are believed to originate from late-time activity of the central engine and can be used to constrain the overall energy budget. In this paper, we collect a sample of 19 long GRBs observed by *Swift*-XRT that contain giant flares in their X-ray afterglows. We fit this sample with a version of the magnetar propeller model, modified to include fallback accretion. This model has already successfully reproduced extended emission in short GRBs. Our best-fittings provide a reasonable morphological match to the light curves. However, 16 out of 19 of the fits require efficiencies for the propeller mechanism that approach 100 per cent. The high-efficiency parameters are a direct result of the high energy contained in the flares and the extreme duration of the dipole component, which forces either slow spin periods or low-magnetic fields. We find that even with the inclusion of significant fallback accretion, in all but a few cases it is energetically challenging to produce prompt emission, afterglow, and giant flares within the constraints of the rotational energy budget of a magnetar.

Key words: accretion, accretion discs – gamma-ray burst: general – stars: magnetars.

1 INTRODUCTION

Gamma-ray bursts (GRBs) are intense explosions that outshine any other source in the gamma-ray sky while they are active (Mészáros 2006). They occur randomly throughout the Universe and are generally categorized into two types (Kouveliotou et al. 1993): short GRBs (SGRBs; lasting < 2 s) and long GRBs (LGRBs; lasting > 2 s).¹ The launch of the *Swift* satellite in 2004 (Gehrels et al. 2004) facilitated a breakthrough in our understanding of GRB physics thanks to its rapid slewing capabilities allowing early and well-sampled observations of afterglows by the X-ray Telescope (XRT) (Burrows et al. 2005a). This led to the formation of a ‘canonical’ X-ray afterglow model consisting of the following phases (Nousek et al. 2006; O’Brien et al. 2006): (i) a steep, early decay; (ii) a plateau; (iii) a late decay; (iv) achromatic jet breaks; and (v) flares. Phases (iv) and (v) do not always have to be present and flares are often superposed on to the plateau phase (Curran et al. 2008).

Flares are a dramatic rebrightening in the X-ray light curve that are seen $\sim 30 - 10^5$ s after the burst trigger (Burrows et al. 2005b;

Beniamini & Kumar 2016) and are observed in approximately half of all GRBs detected by *Swift*-XRT (O’Brien et al. 2006; Curran et al. 2008; Swenson & Roming 2014). Margutti et al. (2011) note that, observationally, there appears to be two different evolutions of X-ray flare luminosity with time. The average luminosity of flares occurring before $t = 1000$ s decreases as $t^{-2.7}$, while the luminosity at later times decreases as $\sim t^{-1}$. Flares are characterized by a fast rise, exponential decay (FRED) profile. The fluence of the largest flares (so-called giant flares) is often comparable to the prompt emission, potentially indicating a common origin between the two (Chincarini et al. 2010). The presence of an underlying continuum that is unaffected by the flare (i.e. the superposition of the flare on the plateau phase) indicates that the flares do not share an emission site with the afterglow (Chincarini et al. 2010), which is believed to be produced by the deceleration of forward shocks in the ambient medium. GRB 050502B contains the first and the largest flare to be observed, rebrightening by a factor of ~ 500 above the continuum (Falcone et al. 2006). The additional energy release observed in giant flares like the one seen in GRB 050502B provide a unique test to constrain the energy budget of GRBs.

There are a variety of models which have been suggested to explain the origin of flares, including: ‘patchy’ shells (Mészáros, Rees & Wijers 1998; Kumar & Piran 2000); refreshed shocks (Rees & Mészáros 1998; Zhang & Mészáros 2002); and density fluctuations

*E-mail: slg44@leicester.ac.uk (SLG); gwy@leicester.ac.uk (GAW); b.gompertz@warwick.ac.uk (BPG)

¹Though the duration of the gamma-rays alone is not able to unambiguously distinguish between the two types, see Bromberg et al. (2013).

(Wang & Loeb 2000; Dai & Lu 2002). The continued central engine (CE) activity model (Dai & Lu 1998; Zhang & Mészáros 2002) is often favoured, since the characteristics of flares are similar to the prompt emission (Chincarini et al. 2010). The new-born millisecond magnetar is a concept that is competing with black holes as the source of power in GRBs, mainly due to its potential as a naturally long-lived central engine (see Bernardini 2015 for a review). In the magnetar model, the rotational energy of a highly magnetized neutron star is tapped via interactions between its intense dipole field and the circumstellar environment (see Zhang & Mészáros 2001). This model has been successfully applied to short (Metzger, Quataert & Thompson 2008; Gompertz et al. 2013; Rowlinson et al. 2013) and long GRBs (Lyons et al. 2010). However, it has a strict energy upper limit imposed by the rotational energy reservoir of the neutron star. This is typically assumed to be $\approx 3 \times 10^{52}$ erg s for a $1.4 M_{\odot}$ neutron star with a 1 ms spin period. The magnetar is expected to be spun-down very rapidly during the prompt emission phase, thereby decreasing the amount of energy available to power a flare (Beniamini & Kumar 2016). However, fallback accretion may augment the magnetar energy budget, as it provides a mechanism to spin the magnetar back up. Recent work by Beniamini, Giannios & Metzger (2017) and Metzger, Beniamini & Giannios (2018) suggests that the extractable energy from an isolated magnetar usable in a GRB is even further reduced. They predict for the same neutron star, the limit would be $\sim 2 \times 10^{51}$ erg making the need for fallback accretion even more severe.

In this paper, we investigate whether flares can be powered by the delayed onset of a propeller regime (Piro & Ott 2011; Gompertz, O’Brien & Wynn 2014), in which in-falling material is accelerated to super-Keplerian velocities via magneto-centrifugal slinging and is ejected from the system. A magnetic propeller provides a path to a smoother emission profile than can be achieved by direct accretion on to a compact object, matching the phenomenology of giant flares more closely. We maximize the available energy reservoir by feeding the disc with fallback accretion (which was successfully used to match the light curves of SGRBs with extended emission in Gibson et al. 2017), following models such as Ekşi, Hernquist & Narayan (2005); Rosswog (2007); Kumar, Narayan & Johnson (2008); Cannizzo, Troja & Gehrels (2011); Parfrey, Spitkovsky & Beloborodov (2016).

In Section 2, we briefly review the magnetar propeller with fallback accretion model used in Gibson et al. (2017). We introduce our sample of long GRBs with significant X-ray flares in Section 3 and present our results and discussion of the fitting procedure in Section 4. We summarize our conclusions in Section 5.

2 THE MAGNETAR MODEL

The propeller regime is defined according to the relationship between the Alfvén radius (where the dynamics of the disc are strongly influenced by the magnetic field, r_m) and the co-rotation radius (where matter in the disc orbits at the same rate as the rotation of the stellar surface, r_c). When $r_c > r_m$, the disc is rotating faster than the magnetic field (assuming the field lines rotate rigidly with the stellar surface) and magnetic torques slow the in-falling material allowing it to accrete. The magnetar gains angular momentum and is spun-up causing r_c to migrate towards the magnetar. This also increases the rotation of the magnetic field lines, causing r_m to migrate outwards. This leads to the opposite case of $r_m > r_c$, so that the magnetic field is rotating faster than the disc. Material is therefore accelerated to super-Keplerian velocities, via direct interaction with the neutron stars magnetic field, and propelled to the light cylinder

radius before being ejected from the system (Piro & Ott 2011). The magnetar loses angular momentum to the ejected material and is spun-down. This is the propeller regime.

In Gibson et al. (2017), we expanded this basic model (Piro & Ott 2011; Gompertz et al. 2014) to include fallback accretion. This was used to successfully reproduce both the prompt emission energy and extended emission in our sample of SGRBs. Full details of the model and results can be found within Gibson et al. (2017). We parametrized the fallback time-scale as a fraction, ϵ , of the viscous time-scale of the disc such that $t_{fb} = \epsilon t_v$. Similarly, the fallback mass budget was defined as a fraction, δ , of the initial disc mass such that $M_{fb} = \frac{3}{2} \delta M_{D,i}$. A mass flow rate of material through the disc – accounting for accretion on to the magnetar, propelling out of the system, and fallback into the disc – was defined as follows:

$$\dot{M}_D(t) = \dot{M}_{fb} - \dot{M}_{acc} - \dot{M}_{prop}, \quad (1)$$

where the fallback rate is defined as

$$\dot{M}_{fb}(t) = \frac{M_{fb}}{t_{fb}} \left(\frac{t + t_{fb}}{t_{fb}} \right)^{-\frac{5}{3}}, \quad (2)$$

using the ballistic time-scale of $t^{-5/3}$ from Rosswog (2007).

Equation (1) and the angular frequency of the magnetar, $\omega(t)$, have been solved over time and from these values the propellered and dipole components of the luminosity (and hence the total luminosity) can be calculated as follows:

$$L_{dip} = -\tau_{dip} \omega \quad (3)$$

$$L_{prop} = -\tau_{acc} \omega \quad (4)$$

$$L_{tot} = \frac{1}{f_B} (\eta_{prop} L_{prop} + \eta_{dip} L_{dip}) \quad (5)$$

where τ_{acc} and τ_{dip} are the accretion and dipole torques, respectively, which have been defined to be positive when the magnetar is spinning up and negative when it’s spinning-down. During spin-up phases, L_{prop} is set to zero. The quantities η_{prop} and η_{dip} represent the efficiencies of the propeller and dipole emission components respectively and $1/f_B$ is the beaming fraction.

We use a Markov chain Monte Carlo (MCMC) simulation package (Foreman-Mackey et al. 2013) to find the optimal values for our nine free parameters: B – magnetic field strength of the magnetar; P_i – spin period of the magnetar; $M_{D,i}$ – disc mass; R_D – disc radius; ϵ – fallback time-scale fraction; δ – fallback mass budget fraction; η_{dip} – dipole energy to luminosity conversion efficiency; η_{prop} – propeller energy to luminosity conversion efficiency; and $1/f_B$ – beaming fraction (please see Appendix A for a discussion of the correlations between these fitting parameters and why a degeneracy treatment is not required). These parameters are defined after the prompt phase has ceased, which has been arbitrarily chosen to be $t = 1$ s. We used 200 ‘walkers’ taking 50 000 steps each and constructed a posterior probability distribution from a Gaussian log-likelihood function and a flat prior function (using the parameter limits given in table 4 in Gibson et al. 2017). Fixed parameters are the viscosity prescription, $\alpha = 0.1$; the speed of sound in the accretion disc, $c_s = 10^7$ cm s $^{-1}$; the ratio $r_m/r_{lc} = 0.9$, which prevents ejected material from exceeding the speed of light; and the dimensionless parameter $n = 1$, which controls how rapidly the propeller emission becomes dominant.

Table 1. The parameters required to perform a cosmological k -correction as described by Bloom et al. (2001). Γ is the photon index; σ is the absorption coefficient calculated from the ratio of counts-to-flux (unabsorbed) to counts-to-flux (absorbed); and z is the redshift given in the literature. For those GRBs with no observed redshift (marked with an *), the mean of the sample in Salvaterra et al. (2012) was used.

GRB	Γ	σ	z
050502B	$1.907^{+0.125}_{-0.098}$	1.11	5.2 ^a
060124	$1.91^{+0.06}_{-0.05}$	1.28	2.297 ^b
060526	$1.98^{+0.17}_{-0.12}$	1.15	3.21 ^c
060904B	$2.05^{+0.15}_{-0.15}$	1.49	0.703 ^d
060929	$3.5^{+1.0}_{-1.4}$	5.79	1.84*
061121	$1.82^{+0.06}_{-0.06}$	1.23	1.314 ^e
070520B	$2.5^{+0.8}_{-0.6}$	1.70	1.84*
070704	$2.3^{+0.5}_{-0.4}$	3.15	1.84*
090621A	$2.09^{+0.26}_{-0.25}$	2.42	1.84*
100619A	$2.30^{+0.16}_{-0.15}$	2.19	1.84*
110709B	$2.01^{+0.06}_{-0.06}$	1.38	0.75 ^f
110801A	$1.99^{+0.11}_{-0.10}$	1.25	1.858 ^g
110820A	$2.5^{+0.6}_{-0.5}$	2.62	1.84*
121123A	$1.85^{+0.11}_{-0.11}$	1.17	1.84*
121217A	$1.97^{+0.11}_{-0.11}$	1.66	3.1 ^h
140817A	$1.803^{+0.103}_{-0.100}$	1.30	1.84*
141031A	$1.85^{+0.32}_{-0.16}$	1.31	1.84*
141130A	$2.0^{+0.4}_{-0.3}$	1.15	1.84*
160425A	$2.47^{+0.20}_{-0.19}$	2.19	0.555 ⁱ

^aAfonso et al. (2011).

^bMirabal & Halpern (2006).

^cBerger & Gladders (2006).

^dFugazza et al. (2006).

^eBloom et al. (2006).

^fPenacchioni et al. (2013).

^gCabrera Lavers et al. (2011).

^hElliott et al. (2014).

ⁱTanvir et al. (2016).

3 SAMPLE OF SWIFT LGRBS WITH GIANT X-RAY FLARES

We have chosen a sample of 19 LGRBs that exhibit significant flares in their X-ray afterglows to study. Since there is no consistent definition of a giant X-ray flare, we selected which LGRBs to study, based on the sample rate of data through the duration of the flare. We require good data coverage near the peak of the flare and a reasonable constraint on the amplitude of the flare so that our fitting routine can properly constrain the free parameters, as such a prominent feature will drive the morphology of the fit.

The data were collected by *Swift*-XRT (Gehrels et al. 2004; Burrows et al. 2005a) and were processed by the UK *Swift* Science Data Centre (UKSSDC²; Evans et al. 2007, 2009). In order to produce bolometric, rest-frame light curves, the data underwent a cosmological k -correction (Bloom, Frail & Sari 2001) and were corrected for absorption using values in Table 1. For those GRBs with no observed redshift, the mean of the sample in Salvaterra et al. (2012) was used (i.e. $z = 1.84$).

4 RESULTS AND DISCUSSION

The best-fittings of the magnetar propeller with fallback accretion model to our LGRB giant flare sample are presented in Fig. 1. The

model provides a reasonable fit to the morphology of the data across the sample, recreating the height and shape of the flare and fitting the emission ‘tail’ in 16 out of 19 GRBs. However in general terms, the model is struggling to meet the general energy budget of the sample which causes some of the parameters to be forced to the extremes of their allowed parameter space (see table 4 in Gibson et al. 2017). The model consistently misses the emission preceding the flare, falling 1–2 orders of magnitude lower than the data. However, this emission is most likely the tail end of the prompt spike, which we do not fit in this paper. The fits which performed the most poorly are GRBs 100619A, 110709B, and 110801A. In the case of GRB 100619A, the model has missed the second flare entirely in favour of fitting to the first flare.³ Currently, our model is unable to fit multiple events like this as it does not contain an underlying flaring mechanism. Instead it describes a large release of energy that fits the general energetics of large flares. The closest approximation to multiple flares our model is currently capable of is a ‘stuttering’ type burst (see Gompertz et al. 2014 and Gibson et al. 2017 for details of burst types). Double flares like this could be achieved using models such as ‘clumpy’ accretion (e.g. Dall’Osso et al. 2017), a self-criticality regime of magnetic reconnection (similar to solar flares, e.g. Wang & Dai 2013), or modulating the fallback rate to no longer be a smooth profile. As discussed in Gibson et al. (2017) in the context of the early time prompt emission, the model struggles to replicate short time-scale variability in GRBs 110709B and 110801A, instead ‘smoothing’ through the main flare and the smaller, preceding flare. This is another feature that may be achievable with a ‘clumpy’ accretion model, self-critical solar flare-like activity, or a modulated fallback rate. Mass would be delivered intermittently, causing outbursts as opposed to the smooth feeding currently modelled here.

The parameter values derived from the best-fitting models are presented in Table 2. Across the sample, we have generally found low-magnetic fields and slow initial spin periods, indicating that the propeller mechanism would not be that strong. A low B -field and fast spin period, or a high B -field and slow spin period have previously been shown to be necessary for an effective propeller (Rowlinson et al. 2013; Gompertz et al. 2014; Gibson et al. 2017). The driving factor behind these parameters is likely to be the duration of the dipole emission. The plateau duration is given by (cf. Zhang & Mészáros 2001):

$$T_{\text{em}} = 10^3 I_{45} B_{p,15}^{-2} P_{i,0}^2 R_{10}^{-6} \text{ s}, \quad (6)$$

where I_{45} is the moment of inertia of the neutron star in units of 10^{45} g cm², $B_{p,15}$ is the dipole field strength in units of 10^{15} G, $P_{i,0}$ is the spin period in ms and R_{10}^{-6} is the neutron star radius in units of 10 km. The dipole emission in our sample typically lasts $\sim 10^5$ s, and assuming $I_{45} = R_{10}^{-6} = 1$, this requires $B_{p,15}^{-2} P_{i,0}^2 \approx 100$. From this we can clearly see that either B must be low, P must be high, or a combination of the two.

The top panel of Fig. 2 shows where the LGRB giant flare sample lies on the spin period-magnetic field plane. 11 GRBs are clustered against the 10 ms upper parameter limit and the majority of the sample have a magnetic field of the order of 1×10^{15} G or less, which are consistent with the theoretical predictions for a magnetar (Giacomazzo & Perna 2013; Mereghetti, Pons & Melatos 2015; Rea et al. 2015). The bottom panel shows where the sample lies

³GRB 100619A exhibits a double flare which is most obvious in the joint BAT and XRT light curve from the UKSSDC’s Burst Analyser found here: http://www.swift.ac.uk/burst_analyser/424998.

²www.swift.ac.uk

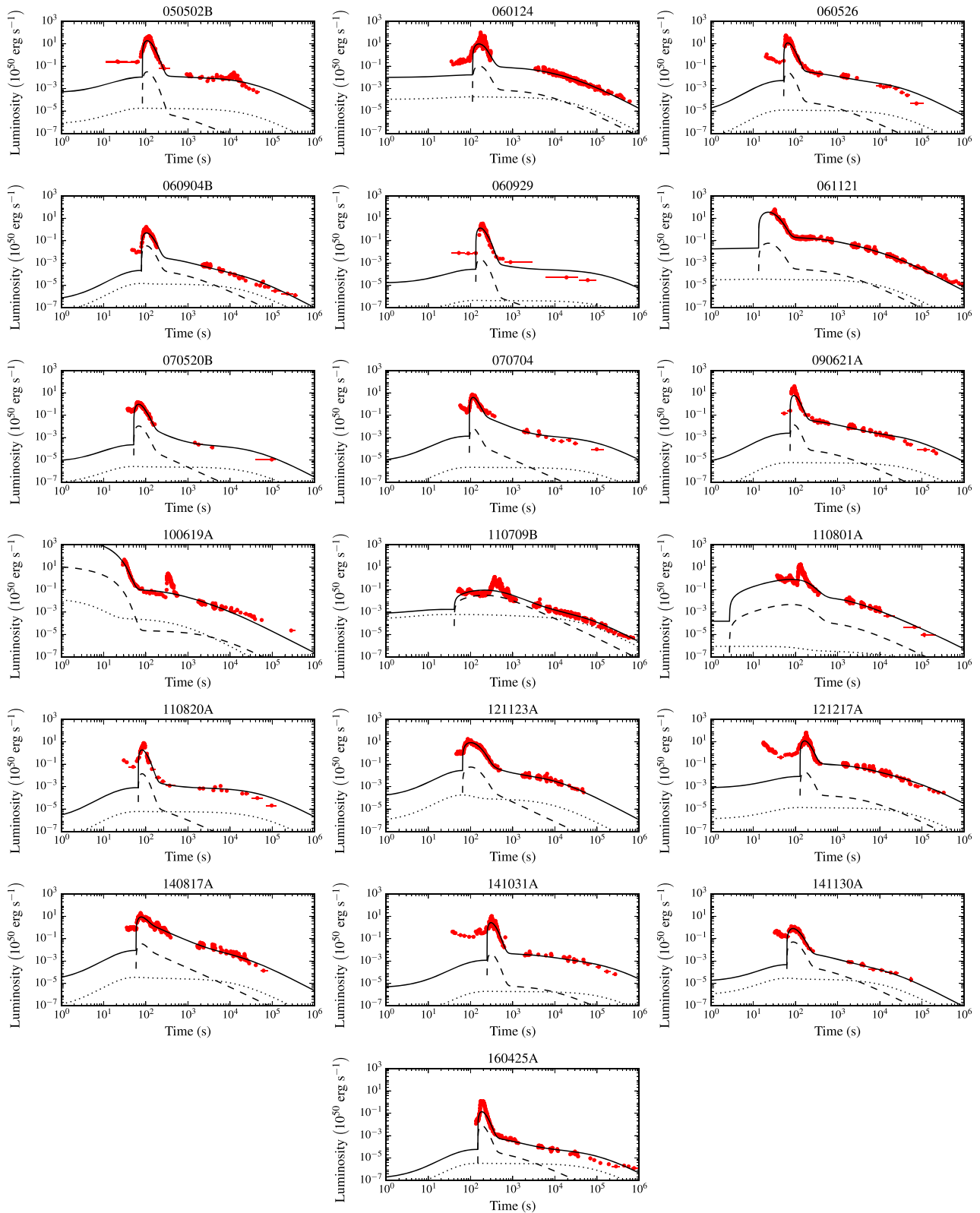


Figure 1. Fits of magnetar propeller model with fallback accretion to LGRB with X-ray flare sample. Red points are *Swift*-XRT data; solid, black line – total luminosity; dashed, black line – propeller luminosity; dotted, black line – dipole luminosity.

in energy space as a fraction of the initial spin energy. The cluster of nine GRBs at the top of the plot all have low B -fields, $\lesssim 1 \times 10^{15}$ G, and slow spin periods, $\simeq 10$ ms, one of the necessary conditions for an effective propeller. The two GRBs over the

upper limit of the spinning neutron star model (GRBs 060124 and 110709B) both have low B and P_1 values and, therefore, have an ineffective propeller mechanism. Hence, the fallback has to compensate to provide the remaining energy. Table 2 shows us that

Table 2. Parameters derived from fits shown in Fig. 1 and the χ^2_{red} goodness of fit statistic. Values marked with an [L] are a parameter limit.

GRB	B ($\times 10^{15}$ G)	P_i (ms)	$M_{D,i}$ ($\times 10^{-2} M_{\odot}$)	R_D (km)	ϵ	δ	η_{dip} (per cent)	η_{prop} (per cent)	$1/f_B$	χ^2_{red}
050502B	$0.47^{+0.02}_{-0.02}$	$4.00^{+0.27}_{-0.22}$	$9.99^{+0.01}_{-0.03}$	217^{+1}_{-1}	$23.24^{+250.16}_{-23.12}$	$(2.14^{+5.25}_{-1.10}) \times 10^{-5}$	1[L]	100[L]	599^{+1}_{-3}	8
060124	$0.165^{+0.006}_{-0.003}$	$0.70^{+0.03}_{-0.01}$	$9.98^{+0.02}_{-0.10}$	417^{+4}_{-5}	$118.79^{+15.78}_{-13.93}$	$(9.83^{+0.87}_{-0.87}) \times 10^{-3}$	1[L]	99^{+1}_{-4}	91^{+7}_{-4}	21
060526	$0.66^{+0.01}_{-0.01}$	$9.97^{+0.03}_{-0.13}$	$9.98^{+0.02}_{-0.09}$	120^{+1}_{-1}	$45.92^{+15.89}_{-13.34}$	$(2.32^{+0.42}_{-0.38}) \times 10^{-4}$	1[L]	100[L]	430^{+17}_{-16}	20
060904B	$0.74^{+0.01}_{-0.01}$	$9.94^{+0.06}_{-0.25}$	$9.97^{+0.03}_{-0.14}$	225^{+2}_{-2}	$30.66^{+8.94}_{-6.91}$	$(9.26^{+1.60}_{-1.43}) \times 10^{-4}$	1[L]	100[L]	14^{+1}_{-1}	10
060929	$0.551^{+0.002}_{-0.002}$	10[L]	$2.58^{+0.02}_{-0.02}$	329^{+1}_{-1}	$10.20^{+3.05}_{-2.72}$	$(2.58^{+0.62}_{-0.63}) \times 10^{-5}$	1[L]	100[L]	599^{+1}_{-3}	419
061121	$1.15^{+0.29}_{-0.22}$	$2.82^{+0.51}_{-0.39}$	$0.96^{+0.19}_{-0.15}$	84^{+2}_{-2}	$127.09^{+16.68}_{-17.55}$	$(1.74^{+0.34}_{-0.33}) \times 10^{-2}$	2^{+1}_{-1}	98^{+2}_{-8}	588^{+12}_{-48}	3
070520B	$1.01^{+0.07}_{-0.05}$	$9.79^{+0.20}_{-0.34}$	$3.31^{+0.90}_{-0.74}$	142^{+4}_{-3}	$0.34^{+2.53}_{-0.24}$	$(1.43^{+2.06}_{-1.06}) \times 10^{-3}$	1[L]	99^{+1}_{-4}	86^{+29}_{-23}	20
070704	$0.43^{+0.01}_{-0.01}$	$9.99^{+0.01}_{-0.03}$	$7.24^{+0.12}_{-0.12}$	188^{+1}_{-1}	$2.02^{+0.93}_{-0.87}$	$(6.57^{+2.43}_{-1.28}) \times 10^{-4}$	1[L]	100[L]	599^{+1}_{-5}	62
090621A	$0.458^{+0.004}_{-0.004}$	$9.99^{+0.01}_{-0.04}$	$9.97^{+0.03}_{-0.11}$	154^{+1}_{-1}	$47.24^{+5.00}_{-4.70}$	$(3.54^{+0.22}_{-0.21}) \times 10^{-4}$	1[L]	100[L]	423^{+12}_{-11}	91
100619A	$7.19^{+2.26}_{-1.72}$	$1.53^{+0.19}_{-0.19}$	$7.04^{+2.79}_{-2.34}$	50[L]	$996.17^{+3.70}_{-16.08}$	$(1.10^{+0.14}_{-0.13}) \times 10^{-3}$	1[L]	83^{+16}_{-24}	394^{+194}_{-171}	124
110709B	$0.13^{+0.47}_{-0.01}$	0.69[L]	$9.93^{+0.07}_{-0.82}$	51^{+1798}_{-1}	$30.93^{+108.34}_{-30.82}$	$0.28^{+12.57}_{-0.04} \times 10^{-2}$	4^{+4}_{-3}	37^{+42}_{-21}	3^{+65}_{-2}	44
110801A	$2.05^{+0.27}_{-0.51}$	$8.47^{+1.47}_{-3.55}$	$0.44^{+0.47}_{-0.13}$	737^{+17}_{-16}	$23.29^{+3.98}_{-3.38}$	$(7.28^{+0.77}_{-0.57}) \times 10^{-2}$	1[L]	91^{+9}_{-27}	174^{+103}_{-112}	37
110820A	$0.48^{+0.01}_{-0.01}$	$9.99^{+0.01}_{-0.06}$	$9.75^{+0.23}_{-0.59}$	134^{+1}_{-1}	$6.13^{+9.64}_{-5.68}$	$(2.66^{+6.49}_{-0.94}) \times 10^{-5}$	1[L]	100[L]	134^{+14}_{-7}	137
121123A	$1.57^{+0.03}_{-0.04}$	$9.77^{+0.22}_{-1.00}$	$9.78^{+0.22}_{-0.79}$	343^{+4}_{-5}	$0.18^{+0.59}_{-0.08}$	$(1.05^{+0.57}_{-0.63}) \times 10^{-2}$	5^{+3}_{-3}	62^{+36}_{-36}	152^{+212}_{-57}	5
121217A	$0.29^{+0.01}_{-0.01}$	$2.78^{+0.16}_{-0.14}$	$9.99^{+0.01}_{-0.04}$	324^{+1}_{-1}	$127.61^{+9.78}_{-9.10}$	$(2.76^{+0.15}_{-0.14}) \times 10^{-3}$	1[L]	100[L]	598^{+2}_{-9}	27
140817A	$0.85^{+0.03}_{-0.04}$	$9.46^{+0.52}_{-1.56}$	$9.94^{+0.06}_{-0.26}$	164^{+4}_{-6}	$1.40^{+0.67}_{-1.28}$	$(1.90^{+7.41}_{-0.32}) \times 10^{-2}$	2^{+1}_{-1}	72^{+26}_{-28}	249^{+156}_{-70}	9
141031A	$0.26^{+0.01}_{-0.01}$	$9.43^{+0.55}_{-1.21}$	$9.98^{+0.02}_{-0.10}$	524^{+3}_{-3}	$144.96^{+53.20}_{-42.31}$	$(2.29^{+0.52}_{-0.48}) \times 10^{-4}$	1[L]	100[L]	597^{+3}_{-11}	21
141130A	$0.94^{+0.35}_{-0.39}$	$5.35^{+4.46}_{-3.49}$	$8.01^{+1.93}_{-5.80}$	228^{+7}_{-11}	$19.28^{+33.27}_{-15.60}$	$(1.42^{+0.63}_{-0.70}) \times 10^{-3}$	1[L]	89^{+11}_{-30}	16^{+73}_{-9}	10
160425A	$0.349^{+0.003}_{-0.004}$	$9.99^{+0.01}_{-0.06}$	$9.97^{+0.03}_{-0.11}$	319^{+1}_{-1}	$22.87^{+3.44}_{-3.10}$	$(1.95^{+0.14}_{-0.14}) \times 10^{-4}$	1[L]	100[L]	$17.3^{+0.6}_{-0.4}$	113

both of these fits exhibit a significant fraction of the initial disc mass falling back on long time-scales compared to the viscous time-scale.

Since $E \propto P_i^{-2}$, initial spin periods of ~ 10 ms reduce the total available energy by a factor of 100. Conversely, in most cases the efficiency of the propeller η_{prop} is forced to 100 per cent, likely in order to compensate for the low total available energy in the model. The mean beaming factor is 303, translating into a jet opening angle of $\theta \approx 4.65^\circ$. This narrow beam is likely a further symptom of a system short of energy. We note at this point that alternative sources of energy which have been ignored here may also make a significant contribution and lower the energy requirements for our model. In particular, we neglect the contribution of the synchrotron emission from the afterglow as the forward shock driven by the initial explosion decelerates. Reprocessing of the dipole radiation in the forward shock will also allow longer lived afterglow emission and enable lower values of P and/or higher values of B compared to the simplified treatment of the dipole applied here (see e.g. Gompertz et al. 2015). Although the relatively long initial spin periods found in the fits are primarily resultant from the need to fit the dipole emission component, we note here that they would be broadly consistent with an episode of magnetar spin-down during the prompt emission phase.

The wide range of values in the fallback parameters ϵ and δ spin the magnetar up at a later period, producing a more effective propeller mechanism. We also find more initial disc masses at the upper parameter limit and with smaller disc radii, which shows that the model is attempting to extract as much energy as possible through high-accretion rates to fuel the flares. The dipole and propeller efficiencies, η_{dip} and η_{prop} , are often pushed to their lowest and

highest parameter limits respectively. This is because the flares produce such large flux increases above the smooth continuum that the model can only reproduce a rise and drop-off of this magnitude by having extremely different efficiencies for the dipole and propeller luminosities, despite this not being observationally consistent.

Although having a mechanism with > 50 per cent efficiency is likely unphysical and observationally inconsistent, it was found to be necessary for both efficiencies to be allowed to vary up to 100 per cent in order for the MCMC simulation to find an acceptable fit with constrained parameters. We ran the MCMC with different combinations of upper limits on the efficiencies and the χ^2_{red} values of 2 arbitrarily chosen runs are presented in Table 3 along with the values for the fits in Fig. 1 for comparison. In each case over all the runs, the MCMC was not able to constrain a value for η_{prop} since each value in the allowed limits had an equally poor χ^2_{red} value as every other. In addition, we ran MCMC simulations that ignored the first 10 s after trigger, which is typically unconstrained by data. We found consistently poor fits, indicating that our conclusions are not dominated by the early (unconstrained) part of the light curve. The dominant limiting factor appears to be the long duration of the emission demanding extreme values of B and P , which forces the other parameters to work around them.

Table 4 presents the values of the Lorentz factors for the X-ray flares in our sample, Γ_X . These have been calculated using equation (7), which comes from Lü et al. (2012) and Mu et al. (2016).

$$\log \Gamma_X = (2.27 \pm 0.04) + (0.34 \pm 0.03) \log L_{X,p,52} \quad (7)$$

where $L_{X,p,52}$ is the peak luminosity of the flare in units of $10^{52} \text{ erg s}^{-1}$.

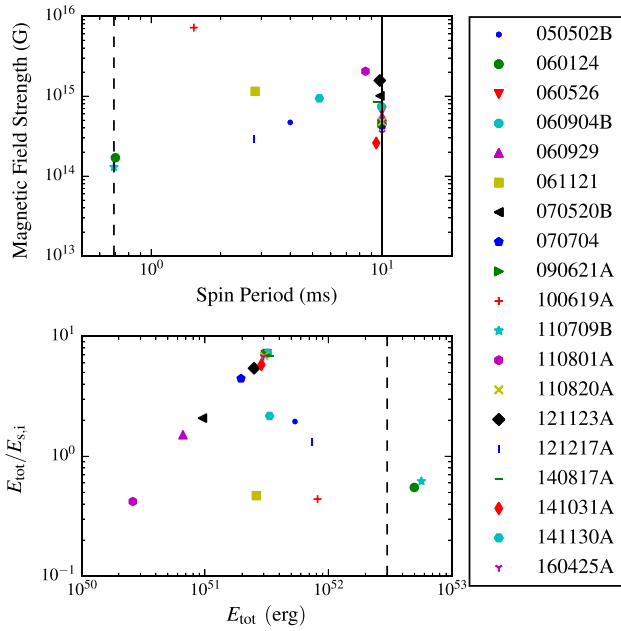


Figure 2. **Top panel:** A plot of the magnetic field strength, B , against the initial spin period P_i of the LGRB giant flare sample. The solid line indicates the upper limit of 10 ms and the dashed line indicates the lower, break-up limit of 0.69 ms for a collapsar (Lattimer & Prakash 2004). Error bars were not included for clarity. **Bottom panel:** A plot showing the ratio of the total energy emitted to the initial spin energy, $E_{\text{tot}}/E_{s,i}$, against the total energy, E_{tot} . The total energy emitted through radiation is calculated by integrating $L_{\text{dip}} + L_{\text{prop}}$ over time of each best-fitting model. The initial spin energy is given by $E_{s,i} = \frac{1}{2} I \omega_i^2$, where $I = \frac{4}{5} M R^2$ is the moment of inertia of the magnetar and ω_i is the initial angular frequency. The dashed line represents the rotational energy reservoir ($\approx 3 \times 10^{52}$ erg s) for a $1.4 M_{\odot}$ neutron star with a 1 ms spin period.

Table 3. The χ_{red}^2 values for fits with different upper limits on the dipole and propeller efficiencies (η_{dip} and η_{prop} , respectively).

GRB	χ_{red}^2		
	$\eta_{\text{dip}} =$ 100 per cent	$\eta_{\text{dip}} =$ 100 per cent	$\eta_{\text{dip}} =$ 50 per cent
	$\eta_{\text{prop}} =$ 100 per cent	$\eta_{\text{prop}} =$ 50 per cent	$\eta_{\text{prop}} =$ 50 per cent
050502B	8	304	891
060124	21	5633	3477
060526	20	3066	6139
060904B	10	125 262	1125
060929	419	119 199	155 054
061121	3	3533	7841
070520B	20	279 130	381 492
070704	62	63 645	24 108
090621A	91	10 819	26 605
100619A	124	11 827	192 847
110709B	44	324 442	66 210
110801A	37	2393	5189
110820A	137	75 866	146 362
121123A	5	18 788	88 012
121217A	27	1607	3425
140817A	9	958	14 149
141031A	21	52 994	3226
141130A	10	214 850	216 761
160425A	113	85 887	212 457

Table 4. Lorentz factor values of the X-ray flare sample, Γ_X , calculated using the $\Gamma_{\gamma} - E_{\gamma, \text{iso}}$ relation in Lü et al. (2012) and Mu et al. (2016). The first column corresponds to the flare Lorentz factor calculated from the *Swift* data, while the second column corresponds to the flare Lorentz factor calculated from the best-fitting models. Since the model misses the second, well-defined flare in GRB 100619A, we have not provided a value of $\Gamma_{X, \text{model}}$ for it. GRBs marked with an * have no redshift and the mean of the sample in Salvaterra et al. (2012) was used.

GRB	$\Gamma_{X, \text{data}}$	$\Gamma_{X, \text{model}}$
050502B	145.75 ± 0.56	105.67
060124	187.85 ± 0.59	84.43
060526	153.04 ± 0.52	90.63
060904B	46.42 ± 0.16	30.71
060929*	59.06 ± 0.11	43.04
061121	158.54 ± 0.50	130.40
070520B*	44.28 ± 0.12	38.04
070704*	75.49 ± 0.17	61.58
090621A*	135.58 ± 0.37	70.55
100619A*	55.24 ± 0.15	—
110709B	43.47 ± 0.13	16.99
110801A	104.93 ± 0.33	36.61
110820A*	77.57 ± 0.19	48.40
121123A*	103.35 ± 0.34	80.52
121217A	161.01 ± 0.49	90.90
140817A*	107.60 ± 0.35	81.28
141031A*	86.33 ± 0.27	54.81
141130A*	42.54 ± 0.14	36.24
160425A	41.62 ± 0.10	19.75

We find our flare sample calculated from the data, $\Gamma_{X, \text{data}}$, is broadly consistent with the findings of Peng et al. (2014) where Γ_X takes values of around $60 \sim 150$. Whereas, the Lorentz factors calculated from the best-fitting models, $\Gamma_{X, \text{model}}$, range from ~ 16 – 130 . While this includes the majority of the range indicated by Peng et al. (2014), the values are often lower than those required by the data especially in the case of the most powerful flares, e.g. GRB 060124. Since the model cannot produce Lorentz factors much greater than ~ 100 , this further highlights that it is struggling to reach the energies demanded of it by the data.

5 CONCLUSIONS

Due to their similarity to the prompt emission, giant X-ray flares in LGRBs are often considered to be evidence of continuing central engine activity. In this paper, we test the feasibility of one of the most natural long-lived central engines: the magnetar model, in which the rotational energy of a highly magnetized millisecond neutron star is released to the surrounding environment via its intense dipole field. Our model for flaring is a magnetic propeller, which accelerates local material via magneto-centrifugal slinging and ejects it from the system. The magnetar is fed by fallback accretion, which maximizes the available energy. We provide fits to a sample of 19 LGRBs with giant flares in their X-ray light curves using MCMC simulations.

Our results show that despite a good phenomenological match of the model to the data, in all but a few cases it is very energetically challenging to explain giant flares in LGRBs using a magnetar alone, especially given the further reduction of usable extracted energy predicted by Beniamini et al. (2017) and Metzger et al. (2018). This has strong implications for any models trying to explain LGRB prompt emission or late X-ray plateaux (Beniamini & Mochkovitch 2017) with a magnetar, as the rotational energy budget appears to not be sufficient for flares without extra emission components

or substantial fallback. However, the energy constraints may be lessened somewhat by the inclusion of the standard synchrotron afterglow and the reprocessing of the dipole emission in the forward shock.

ACKNOWLEDGEMENTS

SLG would like to acknowledge funding from the Weizmann Institute and the University of Leicester. BPG has received funding from the European Research Council (ERC) under the European Union's Horizon 2020 research and innovation programme (grant agreement no 725246, TEDE, PI A. Levan). PTO would like to acknowledge funding from STFC. This research used the Advanced Leicester Information Computational Environment (ALICE) High Performance Computing Facility at the University of Leicester. The work makes use of data supplied by the UKSSDC at the University of Leicester and the *Swift* satellite. *Swift*, launched in November 2004, is a NASA mission in partnership with the Italian Space Agency and the UK Space Agency. *Swift* is managed by NASA Goddard. Penn State University controls science and flight operations from the Mission Operations Centre in University Park, Pennsylvania. Los Alamos National Laboratory provides gamma-ray imaging analysis.

REFERENCES

- Afonso P. et al., 2011, *A&A*, 526, A154
 Beniamini P., Kumar P., 2016, *MNRAS*, 457, L108
 Beniamini P., Mochkovitch R., 2017, *A&A*, 605, A60
 Beniamini P., Giannios D., Metzger B. D., 2017, *MNRAS*, 472, 3058
 Berger E., Gladders M., 2006, *GCN Circ.*, 0, 5170
 Bernardini M. G., 2015, *J. High Energy Astrophys.*, 7, 64
 Bloom J. S., Frail D. A., Sari R., 2001, *ApJ*, 121, 2879
 Bloom J. S. et al., 2006, *ApJ*, 638, 354
 Bromberg O., Nakar E., Piran T. et al., 2013, *ApJ*, 764, 179
 Burrows D. N. et al., 2005a, *Space Sci. Rev.*, 120, 165
 Burrows D. N. et al., 2005b, *Science*, 309, 1833
 Cabrera Lavers A., de Ugarte Postigo A., Castro-Tirado A. J., Gorosabel J., Thoene C. C., 2011, *GCN Circ.*, 0, 12234
 Cannizzo J., Troja E., Gehrels N., 2011, *ApJ*, 734, 35
 Chincarini G. et al., 2010, *MNRAS*, 406, 2113
 Curran P. A., Starling R. L. C., O'Brien P. T., Godet O., van der Horst A. J., Wijers R. A. M. J., 2008, *AAP*, 487, 533
 Dai Z., Lu T., 1998, *A&A*, 333, L87
 Dai Z., Lu T., 2002, *ApJ*, 565, L87
 Dall'Osso S., Perna R., Tanaka T. L., Margutti R., 2017, *MNRAS*, 464, 4399
 Ekşi K. Y., Hernquist L., Narayan R., 2005, *ApJ*, 623, L41
 Elliott J. et al., 2014, *A&A*, 562, A100
 Evans P. A. et al., 2007, *A&A*, 469, 379
 Evans P. A. et al., 2009, *MNRAS*, 397, 1177
 Falcone A. D. et al., 2006, *ApJ*, 641, 1010
 Foreman-Mackey D., Hogg D. W., Lang D., Goodman J., 2013, *PASP*, 125, 306
 Fugazza D. et al., 2006, *GCN Circ.*, 0, 5513
 Gehrels N. et al., 2004, *ApJ*, 611, 1005
 Giacomazzo B., Perna R., 2013, *ApJL*, 771, L26
 Gibson S. L., Wynn G. A., Gompertz B. P., O'Brien P. T., 2017, *MNRAS*, 470, 4925
 Gompertz B., O'Brien P., Wynn G., Rowlinson A., 2013, *MNRAS*, 431, 1745
 Gompertz B. P., O'Brien P. T., Wynn G. A., 2014, *MNRAS*, 438, 240
 Gompertz B. P., van der Horst A. J., O'Brien P. T., Wynn G. A., Wiersema K., 2015, *MNRAS*, 448, 629
 Kouveliotou C., Meegan C. A., Fishman G. J., Bhat N. P., Briggs M. S., Koshut T. M., Paciesas W. S., Pendleton G. N., 1993, *ApJ*, 413, L101
 Kumar P., Piran T., 2000, *ApJ*, 535, 152
 Kumar P., Narayan R., Johnson J. L., 2008, *MNRAS*, 388, 1729

- Lattimer J., Prakash M., 2004, *Science*, 304, 536
 Lü J., Zou Y.-C., Lei W.-H., Zhang B., Wu Q., Wang D.-X., Liang E.-W., Lü H.-J., 2012, *ApJ*, 751, 49
 Lyons N., O'Brien P., Zhang B., Willingale R., Troja E., Starling R., 2010, *MNRAS*, 402, 705
 Margutti R. et al., 2011, *MNRAS*, 417, 2144
 Mereghetti S., Pons J. A., Melatos A., 2015, *Space Sci. Rev.*, 191, 315
 Mészáros P., 2006, *Rep. Prog. Phys.*, 69, 2259
 Mészáros P., Rees M., Wijers R., 1998, *ApJ*, 499, 301
 Metzger B. D., Quataert E., Thompson T. A., 2008, *MNRAS*, 385, 1455
 Metzger B. D., Beniamini P., Giannios D., 2018, *ApJ*, 857, 95
 Mirabal N., Halpern J. P., 2006, *GCN Circ.*, 0, 4591
 Mu H.-J. et al., 2016, *ApJ*, 831, 111
 Nousek J. A. et al., 2006, *ApJ*, 642, 389
 O'Brien P. T. et al., 2006, *ApJ*, 647, 1213
 Parfrey K., Spitkovsky A., Beloborodov A. M., 2016, *ApJ*, 822, 33
 Penacchioni A. V., Ruffini R., Bianco C. L., Izzo L., Muccino M., Pisani G. B., Rueda J. A., 2013, *A&A*, 551, A133
 Peng F.-K., Liang E.-W., Wang X.-Y., Hou S.-J., Xi S.-Q., Lu R.-J., Zhang J., Zhang B., 2014, *ApJ*, 795, 155
 Piro A. L., Ott C. D., 2011, *ApJ*, 736, 108
 Rea N., Gullón M., Pons J. A., Perna R., Dainotti M. G., Miralles J. A., Torres D. F., 2015, *ApJ*, 813, 92
 Rees M. J., Mészáros P., 1998, *ApJ*, 496, L1
 Rosswog S., 2007, *MNRAS*, 376, L48
 Rowlinson A., O'Brien P. T., Metzger B. D., Tanvir N. R., Levan A. J., 2013, *MNRAS*, 430, 1061
 Salvaterra R. et al., 2012, *ApJ*, 749, 68
 Swenson C. A., Roming P. W. A., 2014, *ApJ*, 788, 30
 Tanvir N. R., Xu D., Kruehler T., Malesani D., Fynbo J. P. U., Pugliese G., Levan A. J., Cano Z., 2016, *GCN Circ.*, 19350
 Wang F., Dai Z., 2013, *Nature Phys.*, 9, 465
 Wang X., Loeb A., 2000, *ApJ*, 535, 788
 Zhang B., Mészáros P., 2001, *ApJL*, 552, L35
 Zhang B., Mészáros P., 2002, *ApJ*, 566, 712

APPENDIX A: CORRELATIONS BETWEEN FITTING PARAMETERS

In this Appendix, we address why we have used nine fitting parameters without any contingency for degeneracies between them.

Previously in Gibson et al. (2017), we recreated the four morphologies of bursts the magnetic propeller model could produce as originally described by Gompertz et al. (2014). These types are Type I 'Humped', Type II 'Classic', Type III 'Sloped', and Type IV 'Stuttering'. We chose a synthetic burst to represent each type and ran our MCMC algorithm, using six fitting parameters, to test whether it could accurately reproduce the input values. Figs A1, A2, A3, and A4 are correlation plots generated from those MCMC runs. A strong and consistent correlation between two parameters would indicate that they are degenerate.

While these plots reveal some strong correlations, notably $B - P_i$, $\log(M_{D,i} - \delta)$, $\log(\epsilon - \delta)$, the correlations change strength and shape for each burst type. In the 'sloped' burst case (Fig. A3), the correlation between B and P_i disappears completely because the dipole and propeller luminosity components are indistinguishable from one another in the light curve. Therefore, the parameters cannot always be degenerate with one another since the correlations change as the input parameters are varied and hence a treatment of these degeneracies is not required.

Similar plots for fits to GRBs 060124 and 121217A are presented in Figs A5 and A6, corresponding to the models and values in Fig. 1 and Table 2 respectively. These plots further demonstrate the lack of requirement for a degeneracy treatment between fitting parameters since any correlations have mostly disappeared.

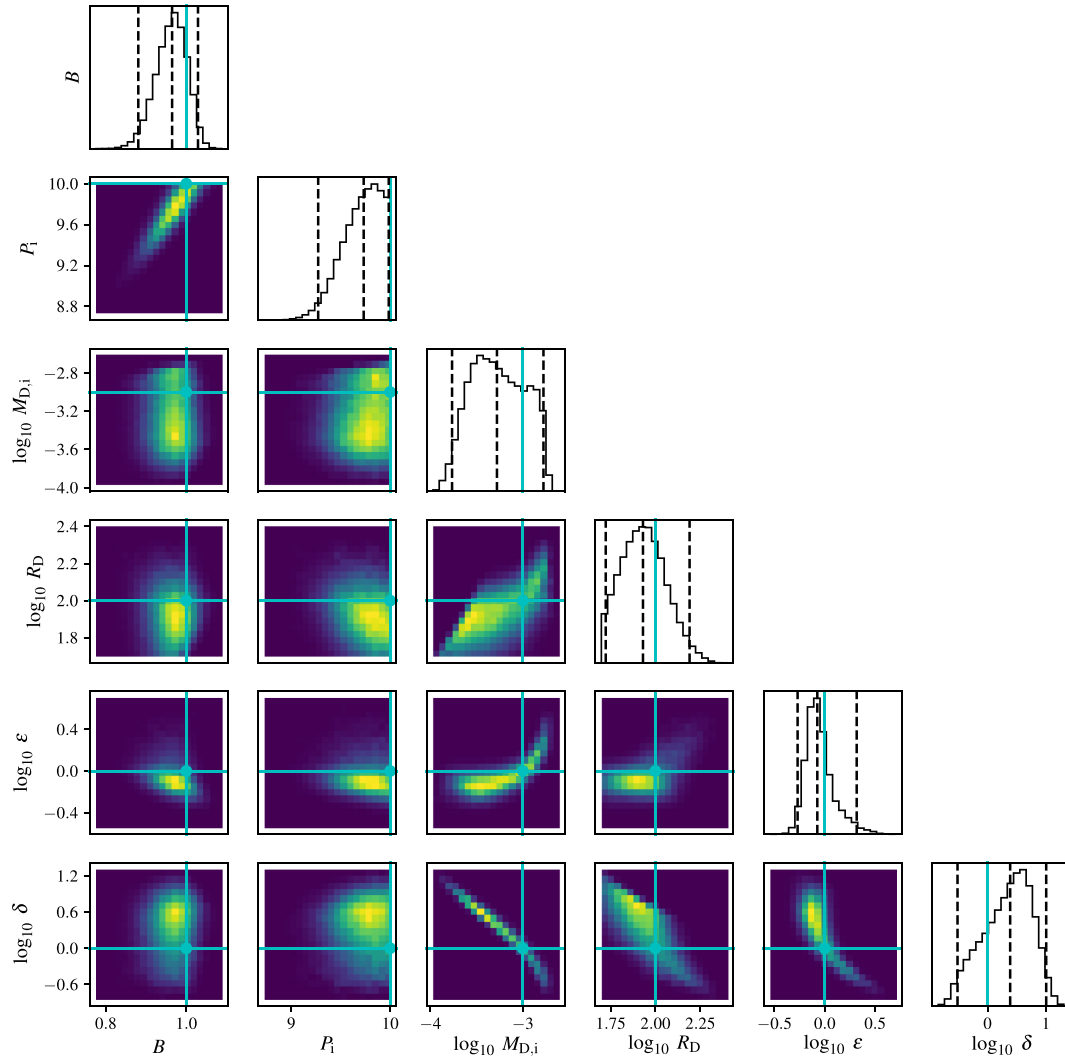


Figure A1. 2D histograms showing the correlations between fitting parameters for a fit to a ‘humped’ synthetic burst. The blue lines and points indicate the true values of the synthetic burst. The 1D histograms show the sampled posterior distribution for each parameter. The dashed lines indicate the median $\pm 2\sigma$ values of the sampled posterior distribution and the blue line indicates the true value of the synthetic curve.

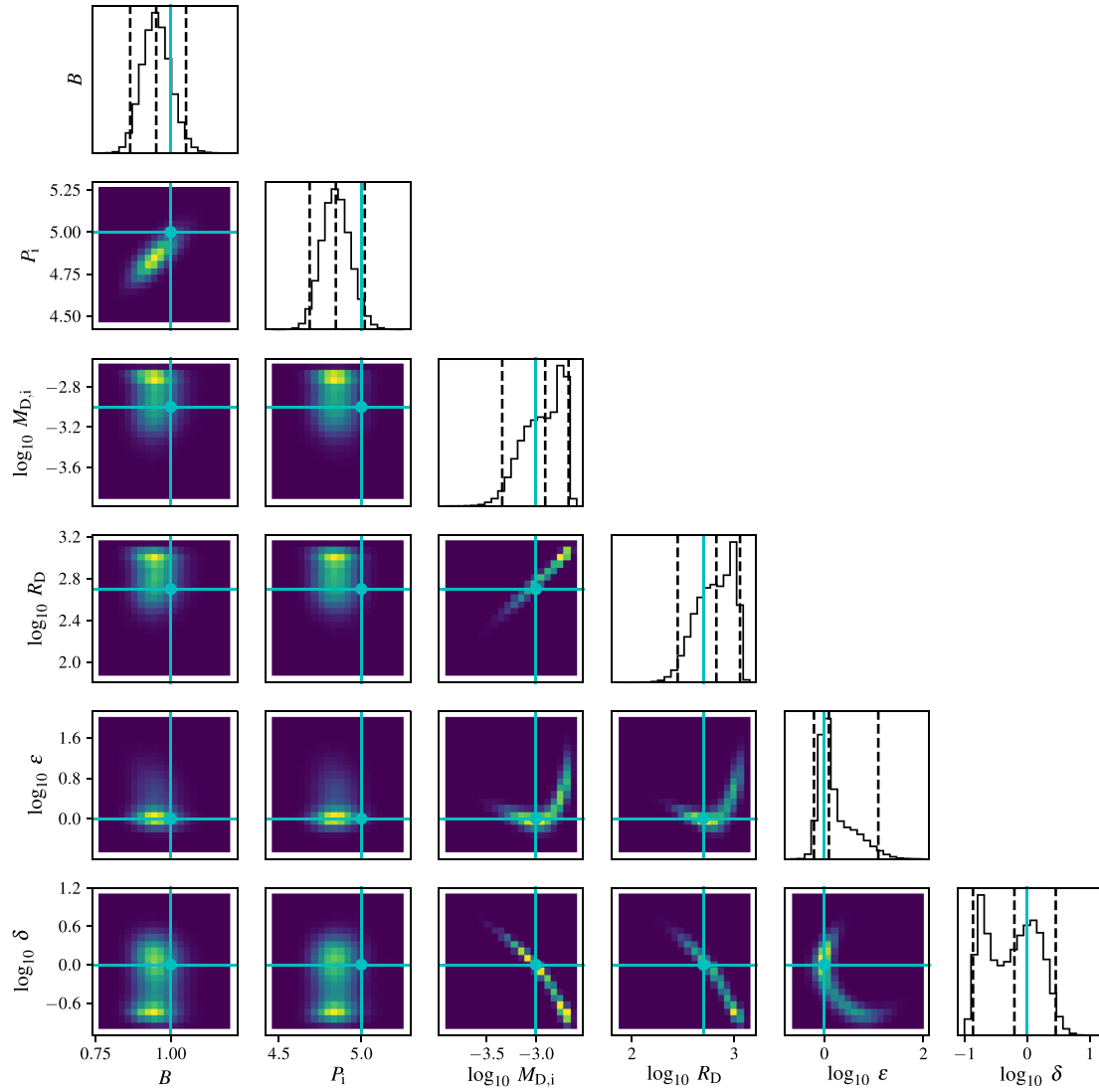


Figure A2. 2D histograms showing the correlations between fitting parameters for a fit to a ‘classic’ synthetic burst. The blue lines and points indicate the true values of the synthetic burst. The 1D histograms show the sampled posterior distribution for each parameter. The dashed lines indicate the median $\pm 2\sigma$ values of the sampled posterior distribution and the blue line indicates the true value of the synthetic curve.

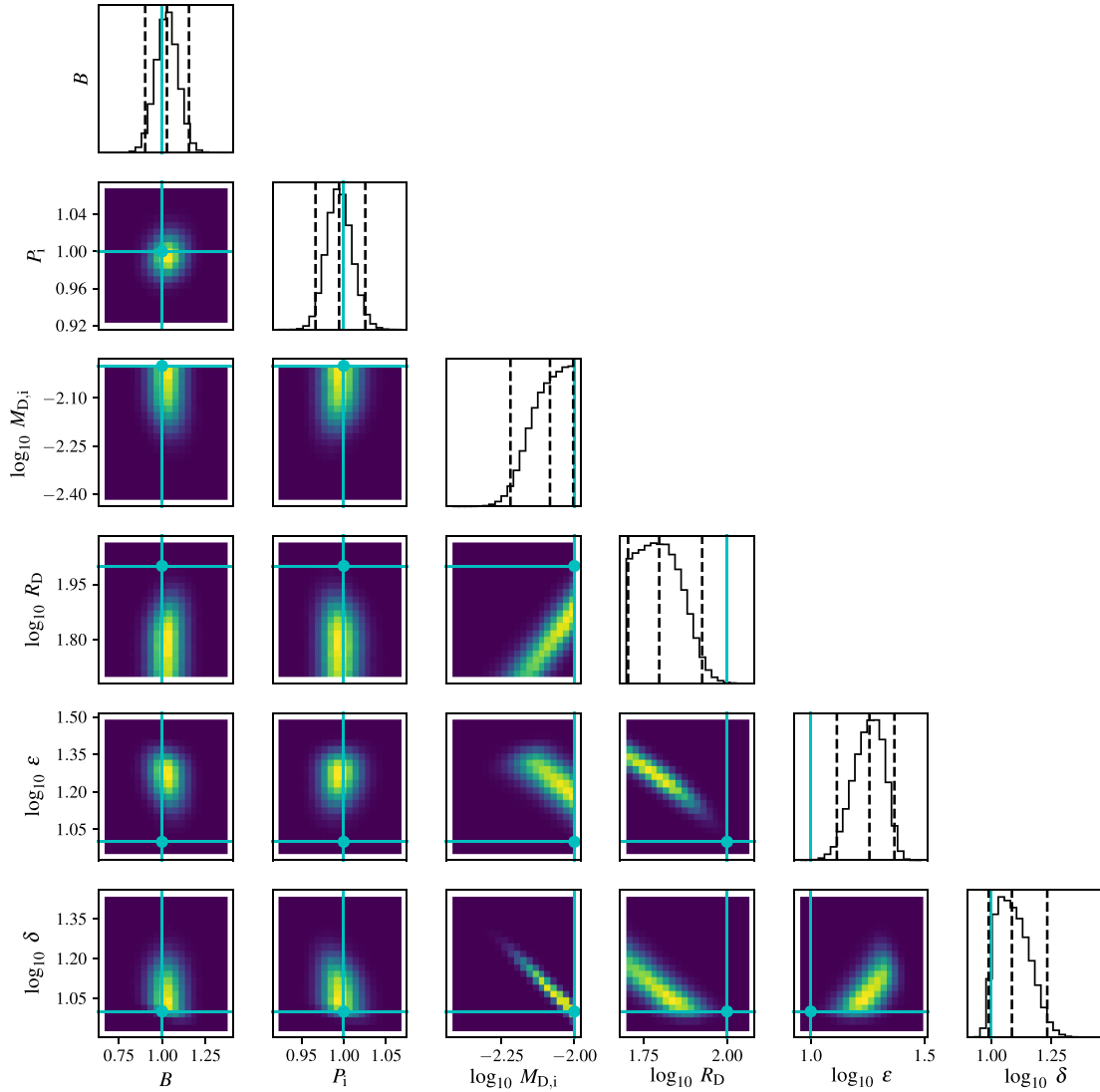


Figure A3. 2D histograms showing the correlations between fitting parameters for a fit to a 'sloped' synthetic burst. The blue lines and points indicate the true values of the synthetic burst. The 1D histograms show the sampled posterior distribution for each parameter. The dashed lines indicate the median and $\pm 2\sigma$ values of the sampled posterior distribution and the blue line indicates the true value of the synthetic curve.

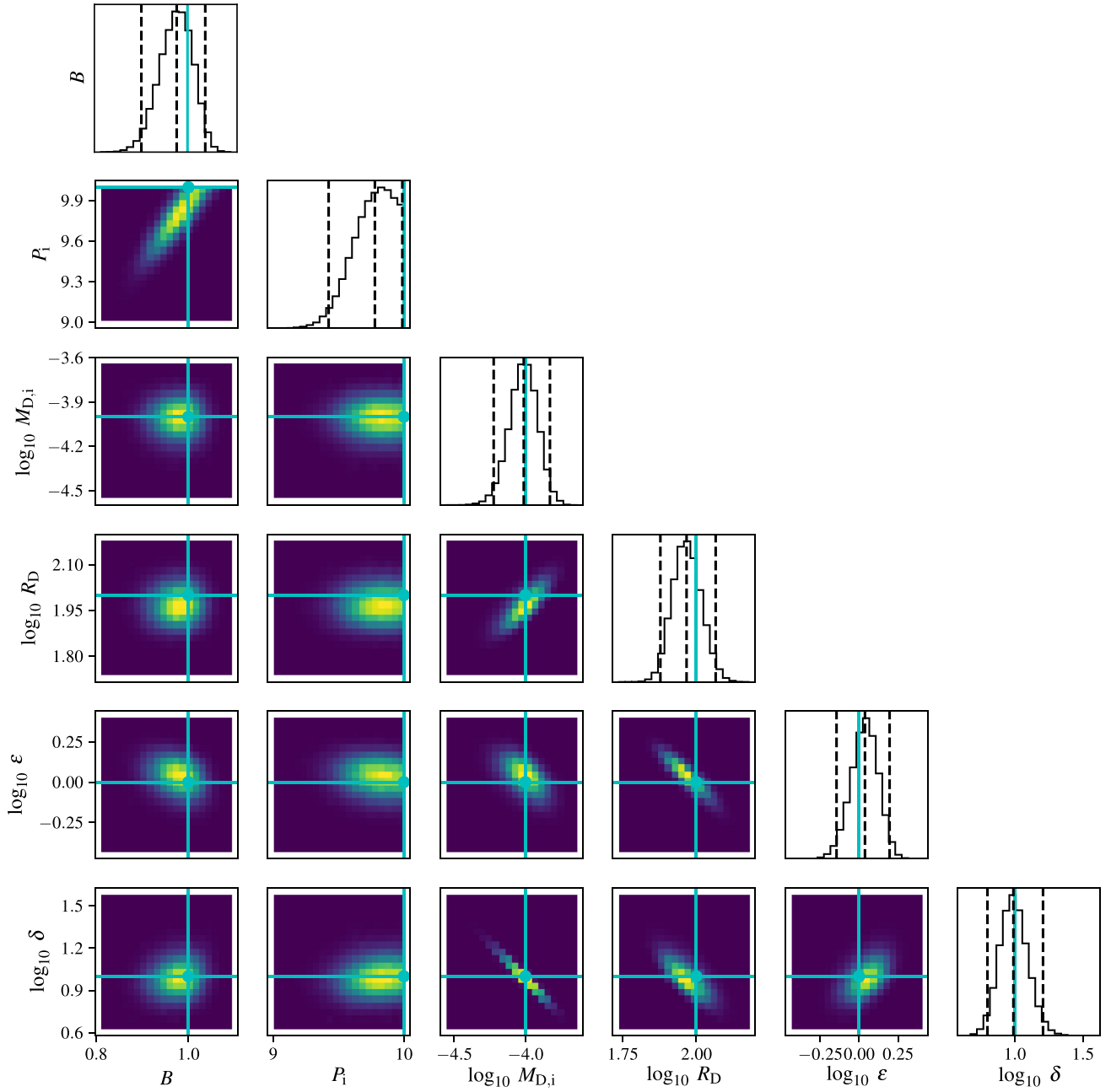


Figure A4. 2D histograms showing the correlations between fitting parameters for a fit to a ‘stuttering’ synthetic burst. The blue lines and points indicate the true values of the synthetic burst. The 1D histograms show the sampled posterior distribution for each parameter. The dashed lines indicate the median and $\pm 2\sigma$ values of the sampled posterior distribution and the blue line indicates the true value of the synthetic curve.

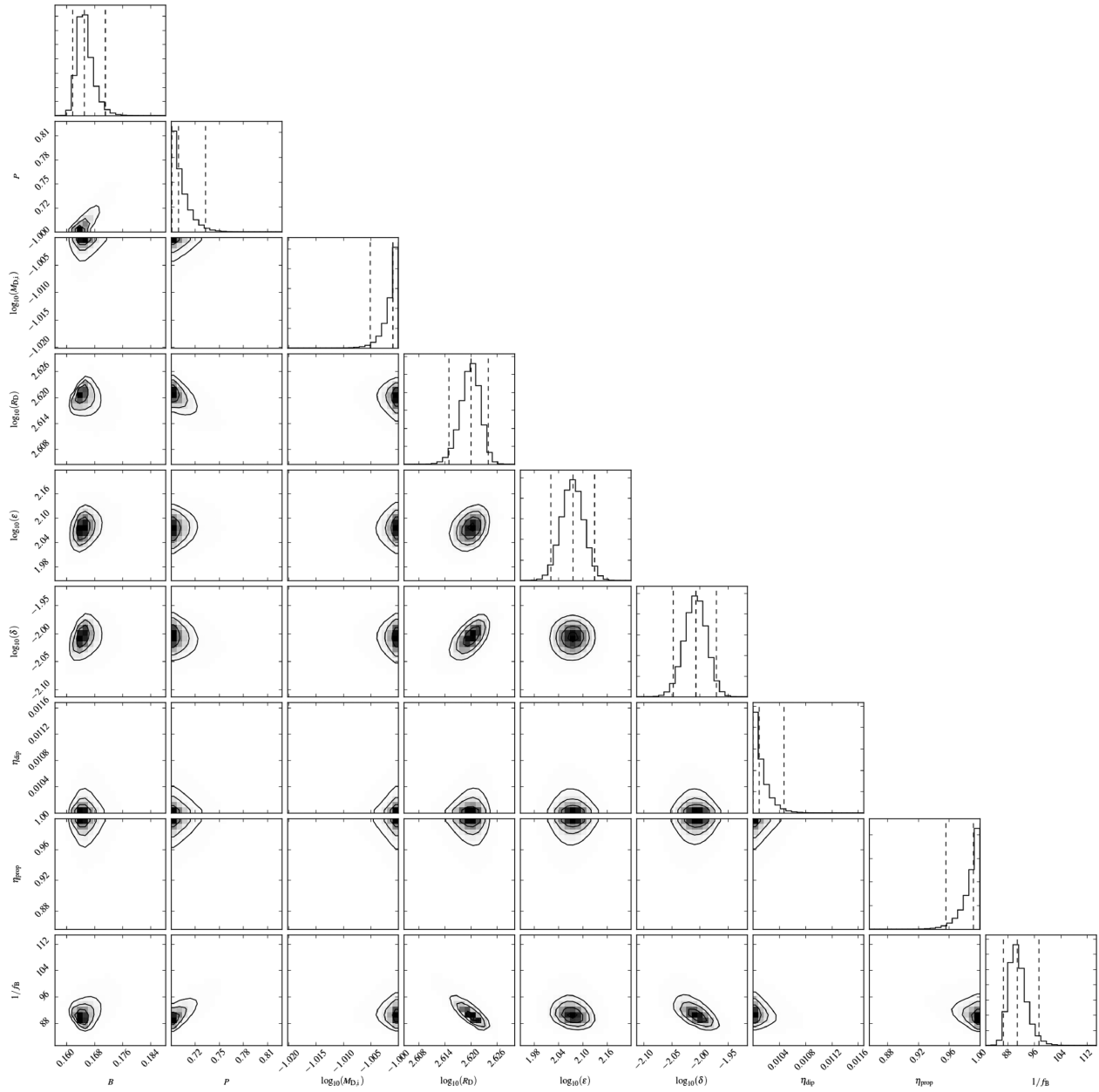


Figure A5. 2D histograms showing the correlations between fitting parameters for the fit to GRB 060124. The 1D histograms show the sampled posterior distribution for each parameter and the dashed lines indicate the median and $\pm 2\sigma$ values corresponding to the values in Table 2.

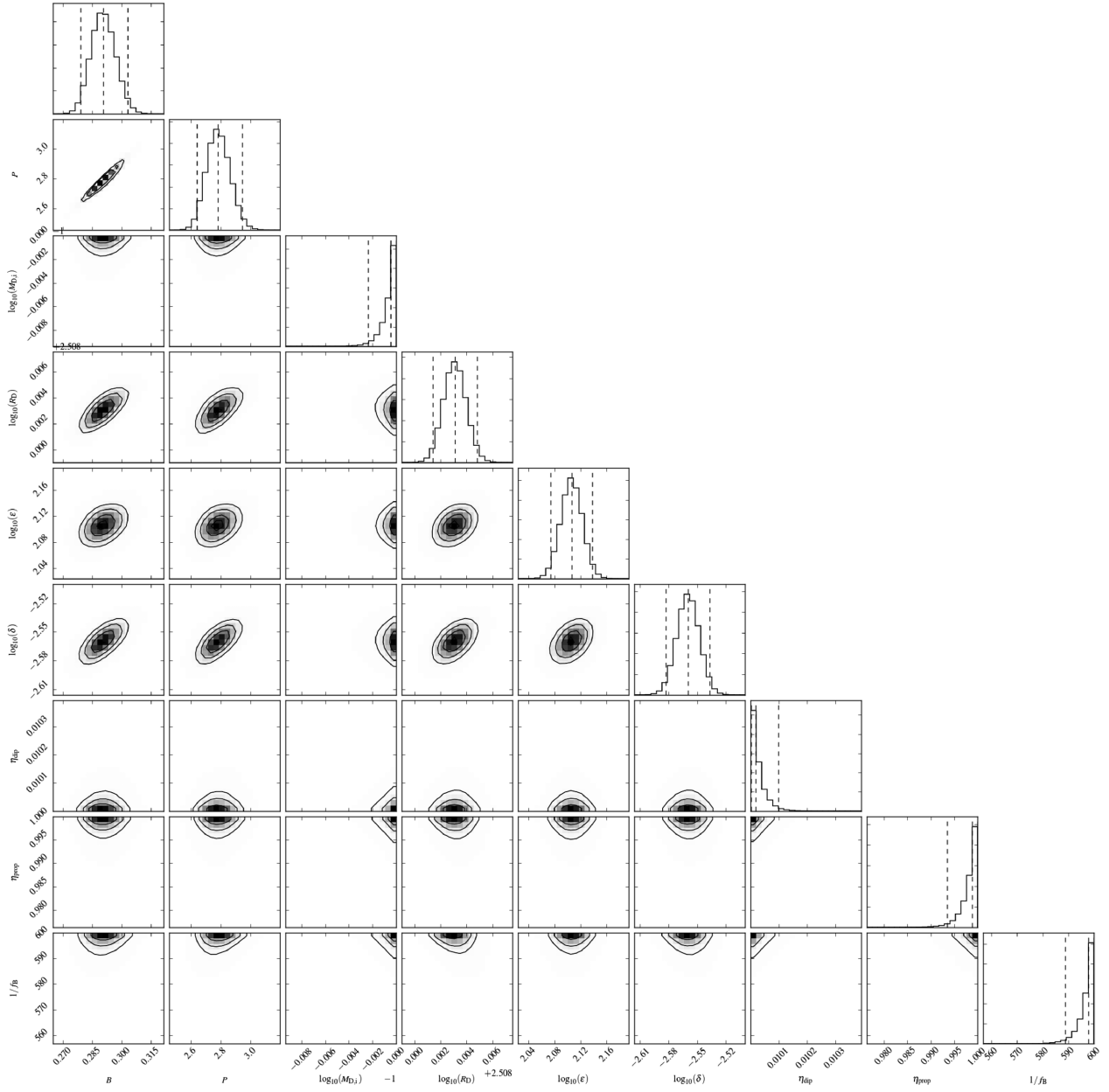


Figure A6. 2D histograms showing the correlations between fitting parameters for the fit to GRB 060124. The 1D histograms show the sampled posterior distribution for each parameter and the dashed lines indicate the median and $\pm 2\sigma$ values corresponding to the values in Table 2.

This paper has been typeset from a $\text{\TeX}/\text{\LaTeX}$ file prepared by the author.